# Imaging of Electrothermal Filament Formation in a Mott Insulator

Matthias Lange,[1] Stefan Guénon,[1,*] Yoav Kalcheim,[2,3] Theodor Luibrand,[1]
Nicolas M. Vargas,[2] Dennis Schwebius,[1] Reinhold Kleiner,[1] Ivan K. Schuller,[2] and
Dieter Koelle[1]

[1] *Physikalisches Institut, Center for Quantum Science (CQ) and LISA+, Eberhard Karls Universität Tübingen, Auf der Morgenstelle 14, Tübingen 72076, Germany*

[2] *Center for Advanced Nanoscience, Department of Physics, University of California—San Diego, 9500 Gilman Drive, La Jolla, California 92093-0319, USA*

[3] *Department of Materials Science and Engineering, Technion—Israel Institute of Technology, Technion City, Haifa 32000, Israel*

(Received 3 July 2021; accepted 5 October 2021; published 12 November 2021)

Resistive switching—the current- and voltage-induced change of electrical resistance—is at the core of memristive devices, which play an essential role in the emerging field of neuromorphic computing. This study is about resistive switching in a Mott insulator, which undergoes a thermally driven metal-to-insulator transition. Two distinct switching mechanisms are reported for such a system: electric-field-driven resistive switching and electrothermal resistive switching. The latter results from an instability caused by Joule heating. Here, we present the visualization of the reversible resistive switching in a planar $V_2O_3$ thin-film device using high-resolution wide-field microscopy in combination with electric transport measurements. We investigate the interaction of the electrothermal instability with the strain-induced spontaneous phase separation in the $V_2O_3$ thin film at the Mott transition. The photomicrographs show the formation of a narrow metallic filament with a minimum width $\lesssim$ 500 nm. Although the filament formation and the overall shape of the current-voltage characteristics (IVCs) are typical of an electrothermal breakdown, we also observe atypical effects such as oblique filaments, filament splitting, and hysteretic IVCs with sawtoothlike jumps at high currents in the low-resistance regime. We are able to reproduce the experimental results in a numerical model based on a two-dimensional resistor network. This model demonstrates that resistive switching in this case is indeed electrothermal and that the intrinsic heterogeneity is responsible for the atypical effects. This heterogeneity is strongly influenced by strain, thereby establishing a link between switching dynamics and structural properties.

DOI: 10.1103/PhysRevApplied.16.054027

## I. INTRODUCTION

The strongly correlated electron system $V_2O_3$ is a prototypical Mott-Hubbard insulator [1]. At room temperature, stoichiometric $V_2O_3$ is a paramagnetic metal with corundum structure, which undergoes a metal-to-insulator transition (MIT) in cooling below about 160 K. The insulating phase is antiferromagnetic with monoclinic structure. Upon heating, the insulating phase undergoes a thermally driven insulator-to-metal transition (IMT) [2–4].

In recent years, there has been a growing interest in utilizing the MIT-IMT in devices based on strongly correlated oxides [5]. One area of application is optical elements, where the MIT-IMT influences the photonic properties [6,7]. Another area of application is resistive switching, where an applied electric current or field induces the IMT and changes the resistance of the device [8,9]. Two technological problems fuel the research in resistive switching. First, there is growing interest in resistive random access memories (RRAMs) as next-generation energy-efficient nonvolatile computer memories. Here, high- and low-resistive states in memristive elements store the data [10–12]. Second, the era of "Big Data" requires methods to access huge data-storage capacities efficiently, which fuels the research field of in-memory computing—combining data storage and logical operations in one chip. At the core of this technology are again memristive elements [13–15]. A subfield of in-memory computing is neuromorphic computing—the search for physical phenomena and concepts that allow the building of artificial neural networks with some of the essential functions of their biological counterparts. Again, memristive elements utilizing resistive switching play a vital role in this emerging research field [16–22].

Several mechanisms have been suggested for resistive switching in Mott insulators. At very high fields ($\gtrsim$ 100 MV/m), Landau-Zener tunneling across the Mott gap increases the free-carrier concentration, which

*stefan.guenon@uni-tuebingen.de

 © 2021 American Physical Society

eventually destabilizes the insulating state, leading to the IMT [23–27]. However, switching with considerably lower fields has been observed in some cases [28–30]. The low-field switching has been attributed to midgap tunneling [31,32], to an electric-field-driven Mott-gap collapse [33], or to a spatially inhomogeneous metal-insulator mixed state [34].

In addition to these mechanisms, in materials exhibiting a thermally driven IMT, a universal electrothermal breakdown must be considered. This instability is not directly related to the Mott-Hubbard physics, but is the result of an electrothermal instability created by the strong temperature dependence of the electric resistivity at the IMT [35–40]. Such an electrothermal instability can lead to resistive switching. When current passes through a highly resistive (insulating) device, Joule heating increases the device temperature. Consequently, small spatial variations in the current density may lead to spatial variations of the local device temperature. The sharp decrease in the resistivity with increasing temperature (at the IMT) acts as a positive-feedback mechanism, which amplifies the evolution of a spatially inhomogeneous state. For electric currents above a certain threshold, this may lead to a runaway effect where more and more current is concentrated in a small section of the device, considerably increasing the local temperature. This runaway effect results in the formation of a highly conductive (metallic) filament connecting the device electrodes. The filament is sustained in the metallic state by the Joule heating concentrated within it, while its surroundings remain in the insulating state at the lower base temperature. In this case, resistive switching is the result of current and temperature redistribution in the device (for an extensive discussion of this phenomenon, see Ref. [41]).

Considering $V_2O_3$ devices, it is possible to suppress the electrothermal effects and enter a purely electronic regime in ultrafast pump-probe experiments [42]. In a study on $V_2O_3$ nanodevices, where size effects and electrode cooling reduced Joule heating, evidence for a dielectric breakdown has been found [30] and, in a recent study, the authors have found that defects in the $V_2O_3$ thin films enhance the efficiency of field-assisted carrier generation and considerably reduce the threshold for a dielectric (nonthermal) breakdown [43]. Electrothermal switching is therefore expected in large and highly pure devices where cooling from the contacts is inefficient and defects do not play a substantial role in the switching process. Moreover, we note that due to the elastic strain and coupling between the structural and the electronic degrees of freedom, $V_2O_3$ thin films on single-crystal substrates have very rich physics on their own [44–49]. Of particular importance is the spontaneous phase separation with herringbone domain structures at the submicrometer scale due to strain minimization at the MIT-IMT [50]; this in turn is likely to also affect resistive switching at the IMT.

Despite major research efforts, the details of the resistive-switching mechanism remain elusive. In particular, for systems with a thermally driven IMT, the question of purely electrically versus electrothermally induced resistive switching has been debated over recent years [9,30,34,36,37,43,51–54]. A fundamental problem for understanding voltage- or current-induced switching is based on the fact that in experiments, the switching is analyzed by electric transport measurements. Naturally, those measurements are only sensitive to the total resistance change of the device. However, the system is inherently strongly inhomogeneous, eventually including a strongly inhomogeneous spatial distribution of current density and temperature. Consequently, knowledge of the spatial distribution of those properties that are relevant for resistive switching is crucial. Hence, it should be highly rewarding to combine electric transport measurements with imaging of filament formation on the submicrometer scale. This may, in particular, provide insights into the relation between strain-induced domain formation and switching-induced filament formation at the MIT-IMT that have hitherto proved to be inaccessible.

In this study, we combine electric transport measurements with cryogenic optical wide-field microscopy (with a spatial resolution of about 0.5 $\mu$m) on $V_2O_3$ thin-film devices. Due to different reflectivity, the photomicrographs yield a strong contrast between metallic and insulating regions, which allows for imaging of the metal-insulator spontaneous phase separation at the MIT-IMT and for the determination of the spatial distribution of local MIT and IMT temperatures. Furthermore, we image the evolution of the formation of highly conducting (metallic) filaments that accompany resistive switching upon sweeping an applied current in the insulating state and recording simultaneously the current-voltage characteristics (IVCs). In this way, the characteristics of the electric transport measurements can be related to the formation, growth, and extinction of metallic filament features at the submicron scale. We find that both the IVCs and the photomicrographs have many characteristics of electrothermal resistive switching due to Joule-heating filament formation. However, we also observe details that we assume to result from the interaction of Joule-heating filaments with the strain-induced varying MIT-IMT temperatures. We develop a numerical model based on a two-dimensional (2D) resistor network, which takes into account the experimentally determined spatial distribution of the local MIT-IMT temperatures. With this model, we calculate the IVCs and the spatial distribution of the current density and temperature upon electrothermal resistive switching and find excellent agreement with experimentally determined IVCs and optically detected filament formation. These results provide a deep understanding of the details of the resistive-switching mechanism at play. In particular, comparing

the spontaneously formed metal-insulator domain structure with the filamentary structures resulting from electrothermal switching also reveals a hitherto unknown interplay between strain and switching.

This paper is organized as follows. After Sec. II, on sample fabrication and the experimental setup, we discuss in Sec. III the thermally driven MIT-IMT in the planar $V_2O_3$ thin-film device under investigation. In addition to resistance $R$ versus temperature $T$ data (Sec. III A), we present photomicrographs at the MIT-IMT, which show characteristic insulator-metal herringbone domain structures (Sec. III B). Then, in Sec. III C, we derive maps of spatially resolved transition temperatures.

The main results are presented in Sec. IV, on resistive switching by current-induced MIT. There, we show IVCs in combination with photomicrographs at the IMT onset (Secs. IV A and IV B) and discuss the experimental results (Sec. IV C). We then present a numerical model (Sec. IV D), based on a 2D resistor network, which shows good agreement in comparison with the experimental results (Sec. IV E). Section V concludes this work.

## II. SAMPLE FABRICATION AND EXPERIMENTAL SETUP

A 300-nm-thick $V_2O_3$ thin film is grown by rf magnetron sputtering of a $V_2O_3$ target on an r plane $(10\bar{1}2)$ sapphire substrate (for details, see Ref. [55,56]). Subsequently, by an optical lithography lift-off process, we prepare several 100-nm-thick Au contact pads on top of the unpatterned $V_2O_3$ film, to define 12 devices on the chip. Each device consists of a 19.5-$\mu$m-long gap between two 20-$\mu$m-wide Au electrodes [see Fig. 1(a)].

We use a wide-field optical microscope [57] with the device mounted in vacuum, in a continuous He gas-flow cryostat. This configuration facilitates electrical transport measurements simultaneously with optical imaging of the device. The microscope has a spatial resolution of about 0.5 $\mu$m. The illumination is monochromatic with a wavelength of 528 nm and the field of view is 500 $\mu$m $\times$ 500 $\mu$m. Optical microscopy allows for imaging the phase separation in the $V_2O_3$ thin film, because the metallic and insulating phases have different reflectivities

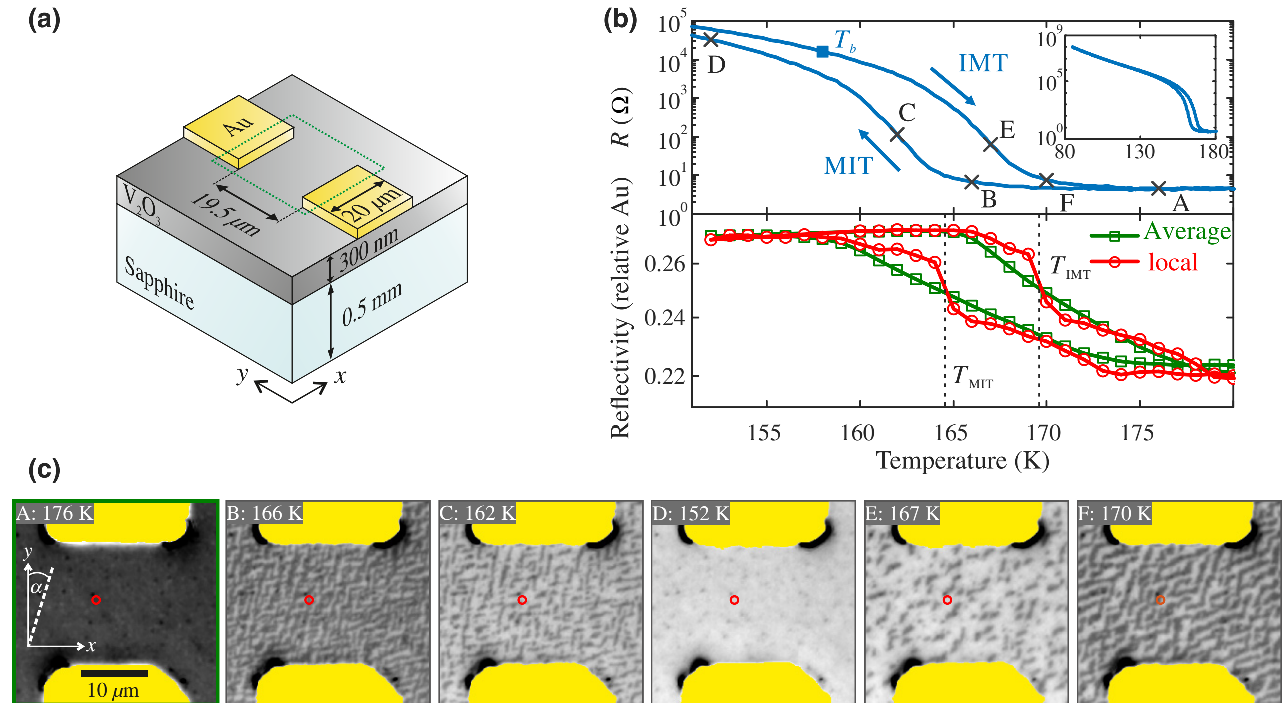


FIG. 1. (a) A schematic view of the planar $V_2O_3$ device under investigation. The two Au electrodes serve as combined current-voltage taps for two-probe electric transport measurements. The dotted green line indicates the area of interest (the field of view of the images is shown in (c)). (b) Resistively and optically detected MIT-IMT. The upper panel shows the electrical resistance $R(T)$ (measured with $I = 5$ $\mu$A); the arrows indicate the sweep direction of the temperature $T$. Data points marked by letters correspond to images shown in (c). $T_b$ indicates the base temperature set for the measurements presented in Fig. 3. The inset shows $R(T)$, including the lowest temperature of the thermal cycle. The lower panel shows the reflectivity versus $T$ of the $V_2O_3$ film normalized to the reflectivity of the Au electrodes. The green curve represents the average over the area of interest, while the red curve represents the reflectivity of a single pixel at the location indicated by the red circles in (c). The vertical dashed lines indicate the local transition temperatures $T_{MIT}$ and $T_{IMT}$, determined for the single pixel. (c) A selection of photomicrographs acquired during one thermal cycle. The Au electrodes are indicated by the yellow areas.

[see Fig. 1(c)]. Note that, counterintuitively, the insulating phase has a higher reflectivity than the metallic phase. The reason for this is that the monochromatic illumination at 528 nm is above the plasma frequency for both phases and therefore the reflectivity contrast is not caused by the concentration of free charge carriers. Instead, $e_g^\pi$ to $a_{1g}$ (lower Hubbard band) [58,59] interband transitions dominate the insulating-phase reflectivity, while transitions from the quasiparticle peak to the $a_{1g}$ upper Hubbard band [55] dominate the metallic phase reflectivity.

We measure the electric transport properties in a two-point configuration with a Keithley 2400 SourceMeter configured as a current source. IVCs are taken from 0 to 20 mA and back to 0 (between 0 and 3.5 mA, the step size is 0.1 mA and then the step size is increased to 0.5 mA, while between 3.0 and 0 mA, the step size is reduced to 0.1 mA).

## III. THERMALLY DRIVEN MIT-IMT

### A. Device resistance

The upper panel of Fig. 1(b) shows the electrical resistance $R$ versus temperature $T$ of the device, acquired with a bias current $I = 5\ \mu$A. The large resistance change at the MIT, by 4 orders of magnitude, is indicative of a high-quality $V_2O_3$ thin film with few defects. Due to the first-order nature of the MIT-IMT, the $R(T)$ curve is hysteretic, with a MIT temperature $T_{\mathrm{MIT}}$ about 5 K below the IMT temperature $T_{\mathrm{IMT}}$. Consequently, for the IVC measurements and imaging presented below, it is vital to prepare a well-defined initial state in order to obtain reproducible results. This is achieved by thermal cycling, i.e., by cooling or by heating to temperatures at which the $V_2O_3$ is in a pure insulating or metallic state, before heating or cooling to the targeted temperature.

### B. Phase separation at the MIT-IMT

We acquire a temperature series of wide-field microscopy images during one thermal cycle with a 1-K step size across the MIT-IMT. Figure 1(c) shows a selection of images from this series. An extended photomicrograph series is included in Appendix A1 (Fig. 5). Capital letters indicate the corresponding temperatures in the $R(T)$ curve [Fig. 1(b), upper panel]. By averaging over the area of interest, we obtain the temperature dependence of the reflectivity of the $V_2O_3$ film, normalized to the reflectivity of the Au electrodes [see Fig. 1(b), lower panel]. The hysteresis in the $R(T)$ curve is well reproduced by the normalized reflectivity versus $T$. The photomicrographs acquired in the hysteretic temperature regime show spontaneous insulator-metal phase separation with herringbone domains [50]. Domain patterns bearing a strong resemblance to those observed here can be found by numerical approximations to the Cahn-Larché equation, which describes the phase separation of a binary mixture in the presence of elastic stress (see Fig. 6 in Ref. [60]). A fast-Fourier-transform (FFT) analysis of the domain pattern is included in Appendix A2 (Fig. 6). The FFT analysis reveals that the domains have two preferred directions; one is at an angle $\alpha \approx 9^\circ$ at the MIT, which switches to $\alpha \approx 22^\circ$ at the IMT, and the second is at $\alpha \approx 79^\circ$, at both the MIT and the IMT. $\alpha$ is the angle between the $y$ axis and the preferred direction [see the coordinates in Fig. 1(c)]. By comparing two optical images taken at the same temperature ($T = 168$ K) in the heating branch (IMT) for two consecutive thermal cycles (see Fig. 7 in Appendix A3), we find that the overall domain geometry (domain size and orientation) for repeated measurements is reproducible, as deduced from the FFT of the images. In real space, however, the domains may form in different locations in every heating cycle, despite a certain level of reproducibility. Interestingly, the heating and cooling cycles show significant differences in domain geometry. These results show that while there is some domain pinning, the local transition temperature depends strongly on cycle-dependent domain nucleation and growth, which changes the local strain distribution. This indicates that the phase separation is not due to growth-induced local inhomogeneities (in, e.g., chemical composition) of the thin film and that the domain configuration is plastic to a certain degree.

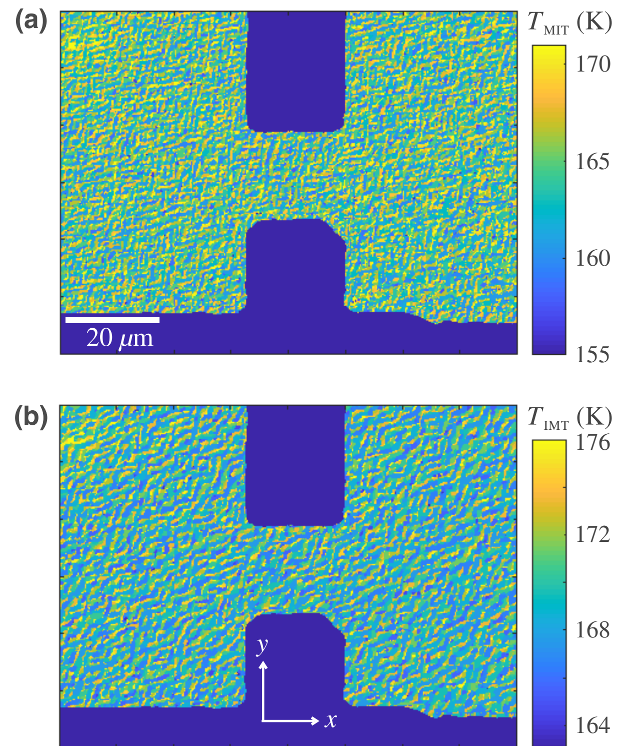


FIG. 2. The local transition temperatures of the $V_2O_3$ thin-film device: (a) $T_{\mathrm{MIT}}$ map; (b) $T_{\mathrm{IMT}}$ map. The large dark blue areas indicate Au electrodes.

In the lower panel of Fig. 1(b), we also include the reflectivity versus $T$ curve for a single pixel, indicated by a red circle in the photomicrographs. The discontinuous steps in reflectivity at the MIT and IMT are indicative of a first-order phase transition [50].

### C. Spatially resolved transition temperatures

By analyzing the steps in reflectivity for every pixel of the photomicrograph temperature series, maps of the local MIT and IMT temperatures $T_{\mathrm{MIT}}$ and $T_{\mathrm{IMT}}$, respectively, with a resolution of 1 K can be derived (see Fig. 2). The maps of $T_{\mathrm{MIT}}$ [Fig. 2(a)] and $T_{\mathrm{IMT}}$ [Fig. 2(b)] show different patches with different transition temperatures, the shape and form of which resemble the herringbone domains in the photomicrographs. We note that the transition temperature maps shown in Fig. 2 constitute a single instance of the local MIT-IMT temperature variation, representing the strain-induced domain structure, but not an actual deterministic transition temperature map. These maps allow us, in the numerical analysis (discussed below), to consider how the strain-induced variation in local MIT-IMT temperatures affects the electrothermal breakdown.

## IV. CURRENT-INDUCED IMT—RESISTIVE SWITCHING

In Fig. 3, we present electric transport data and simultaneously recorded photomicrographs for the current-induced IMT. We also include the results of numerical simulations for direct comparison. Note that we include an animation in Appendix C (Video 1) visualizing the resistive switching for every bias point.

### A. Current-voltage characteristics

Before the measurement, the device is brought into the heating branch [at the base temperature $T_b = 158$ K; cf. Fig. 1(b)] via thermal cycling. Then IVCs are acquired for two consecutive current sweeps [see Fig. 3(a)]. During one sweep, the current increases from 0 mA to the maximum value of 20 mA and decreases back to 0 mA. The arrows in Fig. 3(a) indicate the sweep direction. Starting at the origin of the graph, the IVCs progress almost linearly up to $I \approx 0.5$ mA, which indicates an almost Ohmic resistance. Upon further increase of $I$, the slope of the IVCs increases significantly, i.e., the differential resistance decreases. A section with negative differential resistance follows. A horizontal jump indicative of an instantaneous (within the measurement time scale) reduction of the device resistance interrupts the IVCs at $I \approx 2.5$ mA. In other words, an electrical breakdown of the device causes resistive switching to a low-resistance state. After the jump, the IVCs progress almost vertically with a further increase of $I$. When the current is reduced from its maximum value, the IVCs progress almost vertically down to $I \approx 1.8$ mA, which is below the value of the first horizontal jump. At this bias point, there is a second horizontal jump, indicative of an instantaneous increase of the device resistance, i.e., the device switches back to a high-resistance state. A section with a decreasing slope and a linear section follows.

The IVCs of the first and second sweeps are qualitatively similar. However, the maximum voltage, reached before the voltage jump appears in the upsweep, is reduced for the second sweep. For sweeps following the second sweep (not shown), the maximum voltage does not change any more and the IVCs are almost identical. Thermal cycling restores the IVC of the first sweep. We infer from the reproducibility of the IVC measurements that the observed resistive switching is nondestructive.

In addition to the very pronounced hysteresis in the low-bias-current regime where resistive switching occurs, we observe a small hysteresis in the high-bias regime; i.e., the downsweep branches have lower voltages than the upsweep branches [see the inset to Fig. 3(a)]. Furthermore, in this high-bias regime, the IVCs show small sawtoothlike jumps [see the inset to Fig. 3(a)].

### B. Imaging filaments

Simultaneously with recording IVCs during a current sweep, photomicrographs are acquired. We present a selection of these photomicrographs in Fig. 3(b) (left-hand column) for the second current sweep. The animation in Appendix C (Video 1) shows a movie of the full current sweep.

The following remarks are crucial for interpreting the results. As deduced from the images acquired during the temperature sweeps, metallic and insulating domains have different optical reflectivities, allowing us to assign metallic and insulating resistivities to dark and bright regions of the device, respectively. From Fig. 1(c), we learn that dark areas in the photomicrograph indicate a metallic $V_2O_3$ phase, while the bright areas indicate an insulating phase.

Photomicrograph A in Fig. 3(b) is acquired at bias point A on the upsweep branch of the second current sweep, just before the large voltage jump appears. The photomicrographs acquired between zero bias and bias point A are all identical (see the animation in Video 1 of Appendix C). The $V_2O_3$ thin film between the electrodes is insulating (bright) with several small metallic (dark) inclusions and the device is in a high-resistance state. The metallic inclusions appear after the voltage jump of the first current sweep. Photomicrograph B corresponds to bias point B, immediately after the large voltage jump, indicating an abrupt switching of the device to a low-resistance state. A narrow metallic (dark) filament connects the electrodes at an oblique angle $\alpha$, shunting the insulating film. With further increase of the current, the filament width increases (see photomicrographs B–D) by growing to the right. Bias point D is at $I = 20$ mA, which terminates the upsweep branch. When the current is reduced, the filament splits

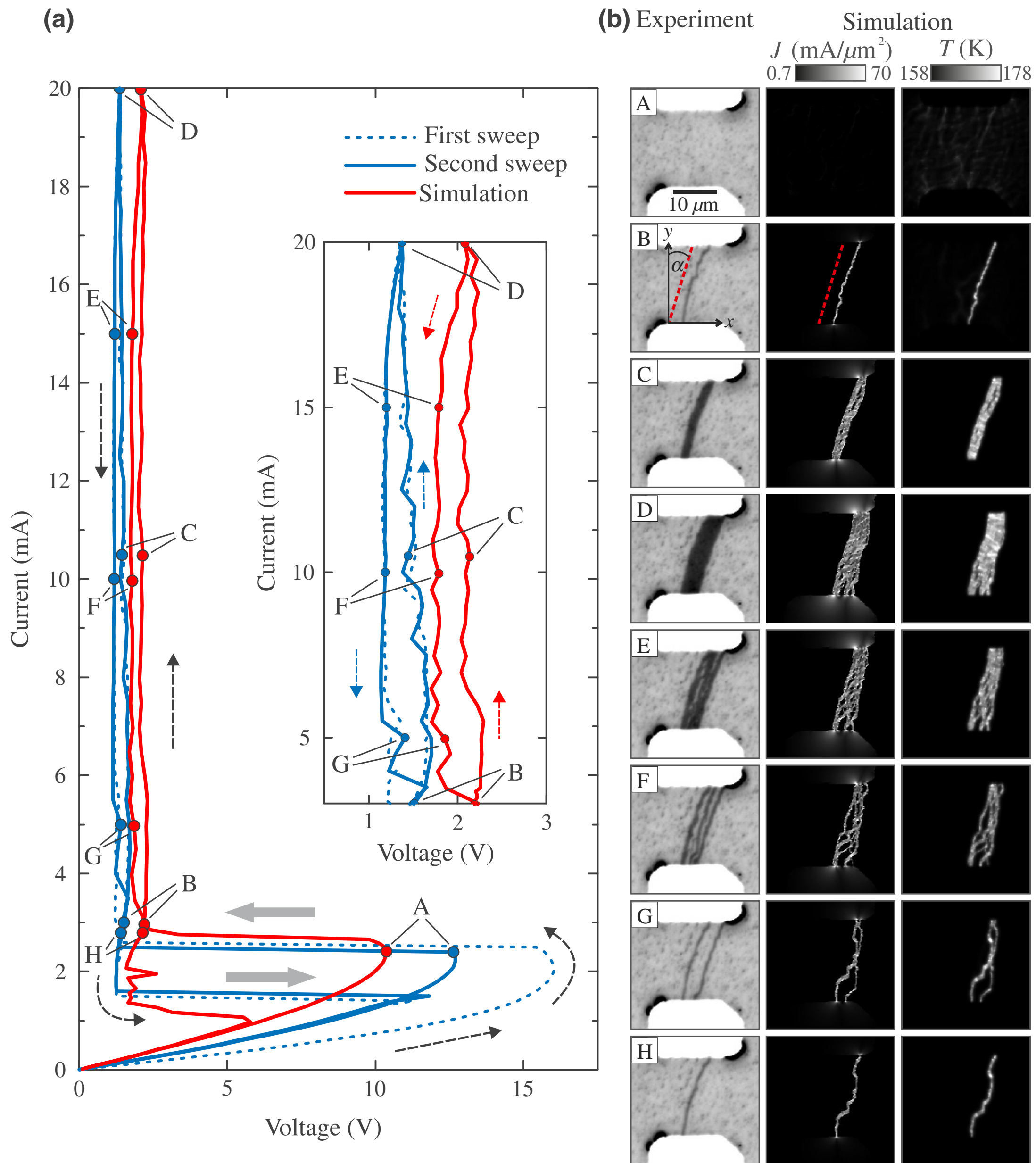


FIG. 3. The electrical breakdown in a planar $V_2O_3$ device at a base temperature $T_b = 158$ K at the onset of the IMT. (a) Measured (blue) and simulated (red) IVCs. The letters label data points for which images are shown in (b). The arrows indicate the sweep directions. The thick gray arrows indicate resistive switching to a low- and high-resistance state, respectively. The inset shows an enlargement of the high-current section. (b) The left-hand column shows a selection of the photomicrographs acquired during the second current sweep. The middle and right-hand columns show a selection of the simulated spatial distribution of the current density $J$ and the local device temperature $T$, respectively. The dashed red lines for images B indicate an $\alpha \approx 17^\circ$ inclination of the filament with respect to the $y$ direction.

into several branches (photomicrograph E). When the current is reduced further, the splitting results in multiple parallel filaments (photomicrograph F). These filaments then disappear one after the other (photomicrographs F–H). Photomicrographs H and B are taken at almost the same current value and are almost identical. Finally, when the current is reduced to a bias point just below the second voltage jump, indicating an abrupt increase of the device resistance, the last remaining filament disappears and the device returns to an insulating high-resistance state (see the animation in Video 1 of Appendix C).

### C. Discussion of experimental results

We derive additional relations (Fig. 4) from the IVC and photomicrographs of the second current sweep, which

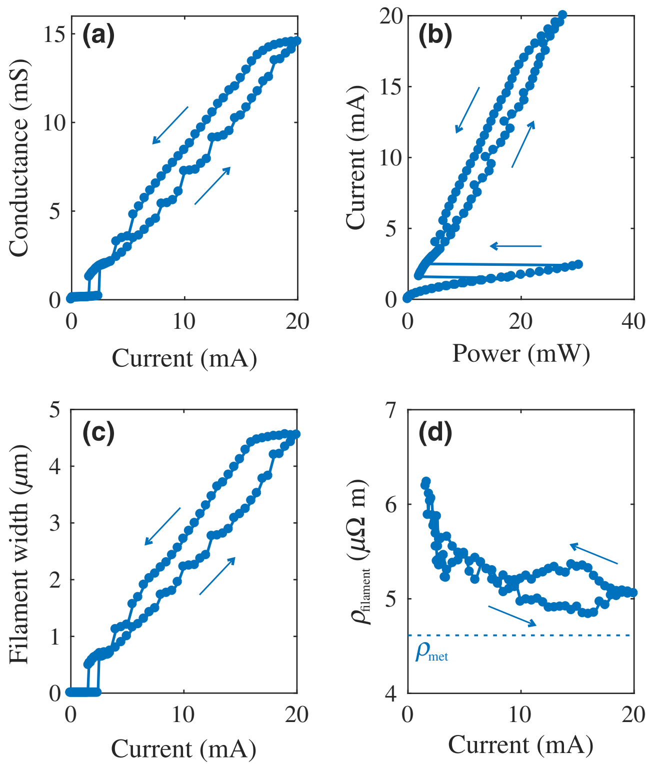


FIG. 4. The relations derived from the IVC and photomicrographs of the second current sweep in Fig. 3: (a) the conductance versus the current; (b) the current versus the power; (c) the estimated total filament width versus the current; (d) the resistivity of the metallic phase, estimated from the filament width, versus the current. The horizontal line indicates the resistivity of the metallic phase $\rho_{\mathrm{met}}$ used in the numerical simulations to obtain agreement with the experimentally measured resistance in the metallic phase.

help us to interpret the results. The derivation of the conductance ($G = I/V$) versus current and the current versus power ($P = I \times V$) relations [Figs. 4(a) and 4(b), respectively] is straightforward. In Fig. 4(c), the filament width is estimated by dividing the dark filament area in the photomicrographs by the filament length, which is estimated by approximating the filament as a straight line. The filament resistivity $\rho_{\mathrm{filament}}$ is derived similarly, assuming that the filament extends throughout the thickness of the $V_2O_3$ film.

Now, we revisit the IVCs and the photomicrographs shown in Fig. 3. The overall behavior of the device is characteristic of an electrothermal breakdown [41]. The increasing slope after the linear (Ohmic) section in the low-bias-current regime, before switching to the high-resistance state, can be explained by a decrease of the device resistance due to Joule heating. According to the $R(T)$ curve shown in Fig. 1(b), close to the IMT an increase in the device temperature results in a considerable decrease in the device resistance. This effect produces the observed back bending of the IVC. The system then becomes electrothermally unstable and the horizontal jump is the result of the formation of an electrothermal filament. Image B of Fig. 3(b) clearly shows the appearance of this metallic filament. The vertical progression of the IVC with increasing $I$ after switching to the low-resistance state is associated with an increase in the filament width [see Fig. 3(b), images B–D]. The second horizontal jump during the return current sweep indicates an abrupt increase of the device resistance associated with the disappearance of the conducting filament (see the animation in Video 1 of Appendix C).

From Fig. 4(b), we learn that resistive switching occurs at maximum power. Considering the IVC of the second sweep [Fig. 3(a)], there is a slight back bending before the jump, indicating resistive switching. In the IVC of the first sweep, this back bending is more pronounced. If resistive switching were purely electric driven, the resistive switching would occur at maximum voltage, which is not the case. This is further evidence for an electrothermal breakdown. According to Fig. 4, in the high-bias regime after resistive switching, the device conductance, power, and filament width have an overall linear current dependence, while the filament resistivity is almost constant. Again, these dependencies are characteristic of an electrothermal breakdown, where the device current flows in a metallic filament and the current controls the width of this filament via Joule heating. Figure 4(d) shows good agreement of the filament resistivity with the resistivity of the metallic phase $\rho_{\mathrm{met}}$ used for numerical simulations (see Sec. IV D). We note that the initial steep decrease of $\rho_{\mathrm{filament}}$ versus $I$ in Fig. 4(d) might be due to the possibility that right after its formation (or before its extinction), the filament does not yet expand throughout the entire film thickness and/or that the filament width is below the spatial resolution of the microscope. In both cases, we would slightly overestimate $\rho_{\mathrm{filament}}$. However, we also note that the independently determined conductance versus current [Fig. 4(a); from IVCs] and filament width versus current [Fig. 4(c); from images] curves match very closely, including the jumps at distinct current values. This indicates that the minimum filament width is very likely not much smaller than what we observe by imaging. Moreover, this again clearly demonstrates how the overall device resistance in the low-resistance state is governed by the optically detected filamentary structures.

We observe atypical effects, which can only be explained by features that are not included in the most simple electrothermal model. First, the filament is not straight along the $y$ axis but, rather, connects the electrodes at an oblique angle $\alpha$ of approximately 17° with respect to the $y$ direction [see image B in Fig. 3(b)]. In a homogeneous medium, one would expect that the shortest possible current path is preferred and the filament should follow the $y$ direction. Second, during the downsweep, the filament first

splits into several branches and then it divides into multiple parallel filaments [see images E and F in Fig. 3(b)]. Because adjacent regions in the film are thermally coupled in the lateral direction, for a homogeneous medium one would expect that, as current decreases, the filament shrinks from its sides, since the filament temperature is highest in its center, so that the colder sides will transition into the insulating state more readily. Third, for high bias currents in the low-resistance state, there is hysteresis in the IVC [see the inset to Fig. 3(a)] and in the conductance, power, and filament width versus current relations (Fig. 4). However, after an electrothermal breakdown in a homogeneous medium without thermal hysteresis, the current should control these parameters without hysteresis in the IVC.

### D. Numerical model

We develop a numerical model to investigate whether the electrical breakdown is electrothermal and whether the phenomena that are atypical for an electrothermal breakdown in a homogeneous medium without thermal hysteresis result from the strain-induced spatial variation of the MIT-IMT temperatures (see Fig. 2). A detailed description, based on Ref. [61], is given in Appendix B.

The numerical model is based on a 2D resistor network (see Fig. 8 of Appendix B1), for which the current distribution is solved via mesh-current analysis, while the thermal properties are modeled with a finite-difference approximation of the time-dependent heat equation. The heat conduction is incorporated using the backward Euler method. Latent heat is included. We account for the thermal coupling to the cryostat cold plate.

The four (or three) resistors of every cell in the 2D network have an individual hysteretic $R(T)$ dependence with the MIT-IMT temperatures corresponding to the experimentally determined values of Fig. 2. Deep in the insulating state, we assume the same resistivity $\rho_{\text{ins}}(T)$ for all cells, which is determined from the measured $R(T)$ curve and, in the metallic state, we assume a constant $\rho_{\text{met}} = 4.6\ \mu\Omega$ m for all cells, also determined from the measured $R(T)$ curve [Fig. 1(b)]. With this approach, the strain-induced variation of the MIT-IMT temperatures is included in the model. For a detailed description, see Appendix B2.

Prior to the simulation of an entire current-sweep sequence, for each pixel the high- or low-resistance state within the hysteretic $T$ range is set, depending on the history. This procedure takes into account, e.g., previous current-sweep sequences and hence can capture history effects in simulations for different current sweeps. For a given bias current value, the mesh-current analysis and the time-dependent heat equation are solved with small time steps until the solution reaches a steady state. Subsequently, the procedure is repeated with an incremented current value. In this way, we calculate the IVC and the spatial distribution of the current density $J$ and the temperature $T$.

### E. Comparison of simulations with experimental results

The simulation results are included in Fig. 3 for direct comparison with the experimental data. The model is numerically stable over almost the whole parameter space, except for a section in the first current sweep after the resistive switching. For this reason, we focus our discussion on the second sweep. We note that the simulation of the first sweep reveals that after return to zero current, some resistors remain in the metallic state. This is consistent with the imaging results, which show that metallic inclusions appear after the first sweep. For the simulation of the second sweep, this information from the simulation of the first sweep is included, which explains why we also find different results in the simulations of different sweeps.

The heuristic numerical model, which includes strain effects in the $V_2O_3$ thin film indirectly via the MIT-IMT temperature maps, reproduces the resistive switching very well. Comparing the simulated IVC with the measured IVC in Fig. 3(a), the threshold currents for resistive switching are very similar and the maximum voltage in the simulation is only 14% smaller than in the experiment. The model reproduces the appearance and disappearance of the metallic filament accompanying resistive switching [see Fig. 3(b) and the animation in Video 1 of Appendix C]. Additionally, the effects, which are atypical for an electrothermal breakdown (discussed above), are also reproduced.

The agreement of the electrothermal model with the experimental results supports the hypothesis that an electrothermal breakdown induces resistive switching. The simulated images for bias points A and B in Fig. 3(b) demonstrate the current and temperature redistribution. As discussed in Sec. I, this redistribution results from a runaway effect driven by electrothermal instability. In particular, the simulation for bias point A already shows an inhomogeneous $T$ distribution within the entire device area prior to resistive switching. After switching to the low-resistance state at bias point B, a single metallic filament appears in the optical image and the simulation shows that the current density is concentrated in this filament, with a local temperature of approximately 20 K above the base temperature $T_b$, while the area outside the filament cools down. At bias point B, the simulation still shows a few filamentary regions with slightly enhanced temperature, while with further sweeping up the bias current, these areas also cool down close to $T_b$.

Remarkably, the simulated data do not only reproduce all the experimentally observed features in the IVCs but also in the shape and direction of the metallic filament.

The filaments in the photomicrographs and the simulation both connect the electrodes at an oblique angle of $\alpha \approx 17^{\circ}$, following roughly one preferred axis of the herringbone domains [see Fig. 1(c)]. The minimum filament width, right before the device switches back to the high-resistance state, is approximately 0.5 $\mu$m, which corresponds to the domain size. However, we note that the value of 0.5 $\mu$m has to be considered as an upper limit, as this is also the spatial resolution of the optical microscope. These observations support the idea that the herringbone domain structure significantly affects the details of resistive switching.

The effects that are atypical of an electrothermal breakdown, such as hysteresis and sawtoothlike jumps in the IVC, filament branching, and splitting, seem to have the same cause: a hysteretic and strain-induced heterogenous electrothermal medium.

Considering the overall shape of the IVCs shown in Fig. 3, the voltage is almost constant in the low-resistance state. This behavior is typical for an electrothermal breakdown, where a Joule-heating filament controls the voltage across the device. Usually, the filament growth with applied current is reversible and the increasing and decreasing current curves are congruent in this bias regime. However, the IVCs are hysteretic [see the inset to Fig. 3(a)]. We argue that the hysteresis in the thermally driven MIT-IMT, i.e., the shift between the MIT and IMT temperatures in $V_2O_3$, is causing this hysteresis in the IVCs. When the device is biased on the increasing current branch, the width of the filament increases and more and more regions undergo an IMT. For electrical bias on the decreasing current branch, the situation reverses, i.e., the width of the filament reduces and more and more regions undergo a MIT. As $T_{\mathrm{IMT}} > T_{\mathrm{MIT}}$, more Joule-heating power is required to drive regions through the IMT on the increasing current branch than on the decreasing current branch, when regions are driven through the MIT. Hence, for a given current $I$, the voltage $V$ is higher in the increasing current branch than in the decreasing current branch.

The sawtoothlike IVC jumps [see the inset to Fig. 3(a)] are due to discontinuous generation and extinction of entire filaments or segments of filaments. We attribute this to filament edge pinning of boundaries between the insulating and metallic phase due to the spatial variation in local IMT temperatures. In particular, the filament does not grow continuously as the current is increased but switches adjacent domains to the metallic state as soon as the dissipated power is sufficient. For increasing currents, only a single filament is visible in the photomicrographs, the width of which increases for increasing currents. For decreasing currents, the expected behavior is that the filament width will decrease continuously. However, the filament branches and splits into multiple filaments (see Fig. 3 and the animation in Video 1 of Appendix C). The varying local MIT-IMT temperatures (see Fig. 2) define percolation paths to which the filaments can lock in. Consequently, when the current is reduced, it distributes along these percolation paths. The geometry of these paths closely resembles the spontaneously forming domain configuration observed during temperature sweeps in the phase coexistence regime at the MIT. For the same reason, the filament is not connecting the electrodes along the shortest path but at an oblique angle. In contrast to the filament in the photomicrographs, the filament in the simulation consists of multiple filaments for biasing on the increasing current branch, although it is more compact than for the decreasing current branch. One explanation is that we cannot resolve these multiple filaments in the photomicrographs due to the limited resolution of the microscope. Another explanation is that the simulation uses transition-temperature maps derived from a series of fixed domain patterns, while in reality the domains are plastic (see the discussion in Sec. III B and Fig. 7 in Appendix A3), i.e., the domain walls can move. Due to this plasticity, there might be a tendency of the domains to merge, which is not reflected in the numerical model.

## V. CONCLUSIONS

We demonstrate electrothermally induced resistive switching in a current-biased planar $V_2O_3$ thin-film device with a base temperature at the onset of the IMT. Photomicrographs show the appearance of a metallic filament that accompanies resistive switching. A model of the resistive switching reveals that the spatial variation in local MIT-IMT temperatures influences the details of the electrothermal breakdown.

The variation of the local MIT-IMT temperatures is the result of strain minimization in the $V_2O_3$ thin film and we conclude that elastic energy influences resistive-switching properties by affecting the filament configuration. Therefore, the influence of strain on the dynamics of switching devices should be taken into account and may allow for novel ways of tuning their properties.

These findings demonstrate the crucial role played by Joule heating and strain effects in this class of memristive devices, which are considered as promising building blocks in neuromorphic computing. Obviously, the approach taken in this work can also be applied to other Mott-insulator systems.

## ACKNOWLEDGMENTS

This work was supported as part of the Quantum Materials for Energy Efficient Neuromorphic Computing (Q-MEEN-C) Energy Frontier Research Center (EFRC), funded by the U.S. Department of Energy, Office of Science, Basic Energy Sciences under Award No. DE-SC0019273. Part of the fabrication process was done at the San Diego Nanotechnology Infrastructure (SDNI)

of University of California—San Diego, a member of the National Nanotechnology Coordinated Infrastructure (NNCI), which is supported by the National Science Foundation under Grant No. ECCS-1542148. Y.K. acknowledges the support of a Norman Seiden Fellowship in Nanotechnology and Optoelectronics.

M. L. and S. G. contributed equally to this work.

## APPENDIX A: PHASE SEPARATION AT THE MIT-IMT

This appendix provides further details on the phase separation of the investigated $V_2O_3$ film across the MIT and the IMT.

### 1. Evolution of domain configurations across the MIT-IMT

Figure 5(b) shows a more detailed series of photomicrographs at temperatures $T$ across the MIT-IMT. The $R(T)$ curves [Fig. 5(a)] are acquired with a bias current $I = 5\ \mu$A. The capital letters indicate the acquisition temperatures of the photomicrograph series. The $R(T)$ curves show a 4-order-of-magnitude change of $R$ across the MIT-IMT, with a thermal hysteresis of approximately 5 K between the cooling and heating branches. The minimum temperature within the thermal cycle is 80 K.

The transition between the two phases progresses through the formation of domain patterns with dark and bright contrast that are identified as metallic and insulating regions, respectively. Starting from a homogeneous metallic state (A: 176 K), small insulating islands begin to form (B: 170 K) that grow and connect to form a herringbonelike domain pattern (C: 168 K and D: 166 K). At this point, the metallic domains still provide continuous paths connecting the electrodes. These get disconnected when the temperature is further decreased (E: 164 K and F: 162 K), which goes along with a steep increase in resistance, as the current now has to flow through parts of the film that are in the insulating phase. At even lower temperatures (G: 161 K, H: 160 K, and I: 158 K), the $V_2O_3$ film is in a state where metallic patches are embedded within an insulating matrix. The size of the metallic domains decreases with decreasing temperature until the sample is in an almost homogeneous insulating state (J: 152 K).

The heating branch shows a slightly different behavior. Beginning from the insulating state (K: 160 K), small metallic islands appear (L: 164 K and M: 166 K) that connect to elongated domains (N: 167 K and O: 168 K). These domains are wider than the domains in the cooling branch and have a different preferred direction. Upon further increase of the temperature, more metallic domains appear and long metallic paths are created that eventually form continuous metallic paths that connect the electrodes (P: 170 K). The metallic regions grow (Q: 172 K and R: 174 K) until only isolated insulating patches are left

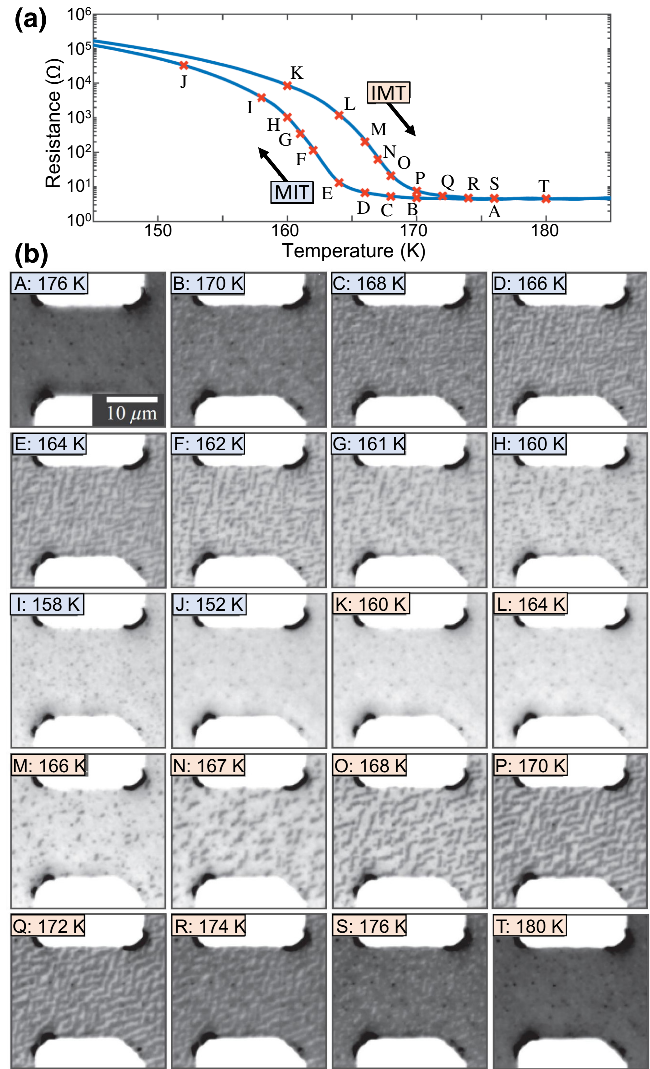


FIG. 5. The phase separation in $V_2O_3$ at the MIT-IMT: (a) $R(T)$ curves; (b) images acquired at the points, labeled A–T in (a), during cool-down and warm-up of the sample.

(S: 176 K). Eventually, the film arrives in a homogeneous metallic state (T: 180 K).

### 2. Directionality and periodicity of the domain patterns

The preferred direction of the domains and their periodicity can be estimated from the FFT) of the optical images. This is shown for selected temperatures in Fig. 6. Angles are measured clockwise with respect to the vertical axis, i.e., they correspond to the definition of $\alpha$ for optical images in the main text. The FFT of the domain configuration in the MIT [Figs. 6(a) and 6(b)] clearly shows four peaks that correspond to directions of 99° and 169°, with a mean periodicity of 1.3 $\mu$m at 166 K and 1.5 $\mu$m at 162 K. The preferred orientations of the long axis of the domains

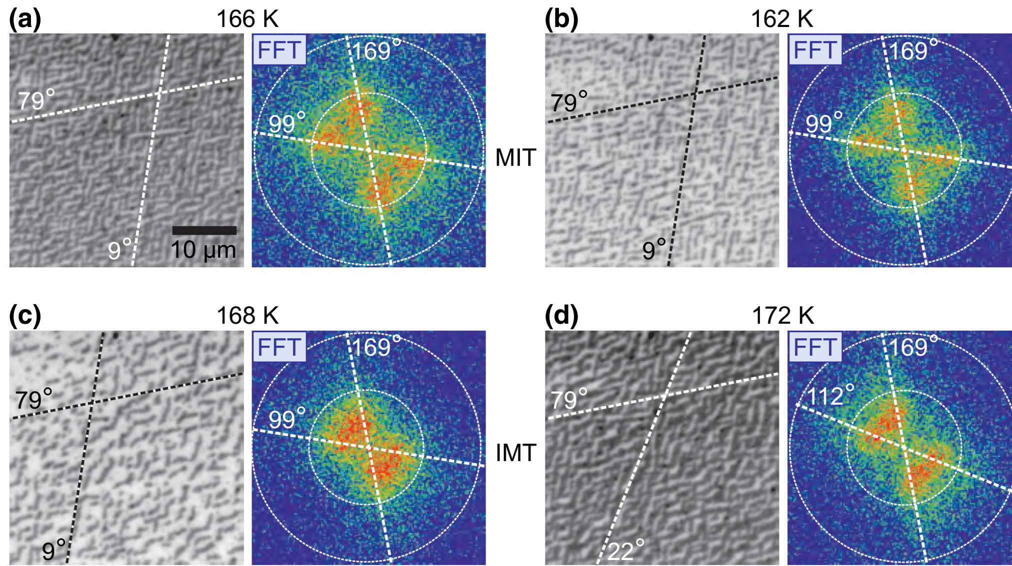


FIG. 6. The domain configuration (left) and FFT (right) for selected temperatures of (a) 166 K and (b) 162 K in the cooling branch (MIT) and (c) 168 K and (d) 172 K in the heating branch (IMT). The dashed lines highlight the predominant directionality of the long axis of domains in the real-space images and in which the peaks occur. The angles are measured clockwise with respect to the vertical axis. The inner (outer) circles in the FFT correspond to a spatial frequency of $1/\mu$m ($2/\mu$m).

in real space are perpendicular to the directions found in the FFT and are indicated by the broken lines at 9° and 79° in the optical images. Figures 6(c) and 6(d) show the domain configuration and FFT for temperatures of 168 K and 172 K in the IMT. At $T = 168$ K, it is not possible to distinguish the peaks of the 99° and 169° axes in the FFT. However, the real-space image at 168 K shows that many of the domains are still oriented along the 9° and 79° axes, while some domains have an orientation that lies in between these axes. At 172 K, on the other hand, only a few domains are oriented along the 9° axis and the preferred directions become 22° and 79°, which is observed in the FFT as a narrowing of the peaks in the angular direction. The mean periodicity of the domains in the heating branch (IMT) is found to be 2.2 $\mu$m at 168 K and 1.8 $\mu$m at 172 K.

### 3. Reproducibility of the domain configuration

Figures 7(a) and 7(b) show the domain configuration at 168 K in the heating branch for two subsequent measurement runs. A complete thermal cycle (heating to room temperature and cooling to 80 K) separates the two images. While the overall density of metallic domains is similar, the domain patterns differ significantly. For comparison, a color-coded superposition of the images in Figs. 7(a) and 7(b) is shown in Fig. 7(c). Metallic domains that are present in both Figs. 7(a) and 7(b) appear dark. Domains that are present only in Fig. 7(a) are represented in green, while those that are present only in Fig. 7(b) are represented in red. It is apparent that the domain configuration for repeated measurements is neither deterministic nor random. The same holds true for other temperatures in both the MIT and IMT. This indicates that the phase separation is not due to growth-induced local inhomogeneities of the film—e.g., in chemical composition—which could lead to a spatially varying transition temperature but, rather, is caused through minimization of local strain, as proposed by McLeod *et al.* [50].

## APPENDIX B: NUMERICAL MODEL

This appendix describes the numerical model, which is used to simulate the IVCs and spatial distribution of temperature $T$ and current density $J$ in the $V_2O_3$ films. This description is based on chapter 5.4 in Ref. [61].

### 1. Resistor network and mesh-current analysis

To calculate the current distribution, the sample is approximated by a 2D resistor network that is constructed from a square primitive cell with edge length $\Delta x = \Delta y$ that contains one node and four resistors. The resulting resistor network, obtained by assembling $n$ primitive cells in the $x$ direction and $m$ primitive cells in the $y$ direction, is shown in Fig. 8. The four resistors within each primitive cell with index $i,j$, with $i \in \{1, m\}$ and $j \in \{1, n\}$, are assigned the same resistance $R_{i,j}$. The resistors at the left and right edges of the resistor network are truncated, making the boundary insulating, and a perfectly conducting wire connects the bottom and top edges to the current

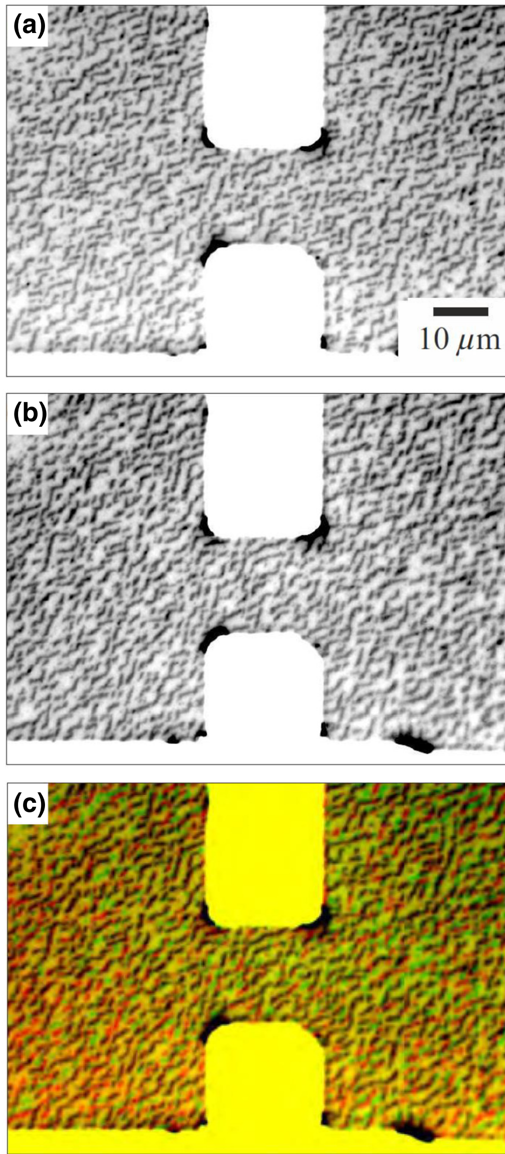


FIG. 7. The reproducibility of the domain configuration. (a),(b) Optical images, recorded at 168 K in the heating branch for two subsequent runs with a full thermal cycle in between. (c) The color-coded superposition of images from (a) and (b). Metallic domains that are present in both (a) and (b) appear dark. Metallic domains only present in (a) are green, while those only present in (b) are red. Insulating domains present in both micrographs are shown in yellow.

source. The loops formed by four neighboring nodes and the resistors between them are called essential meshes.

For the complete resistor network, one obtains a set of $a = (n-1)(m+1)$ equations for $a$ essential meshes plus the equation for the current source mesh, which serves as a boundary condition. This set of equations is assembled into a $(a+1) \times (a+1)$ matrix $\mathbf{W}$, so that the equation system

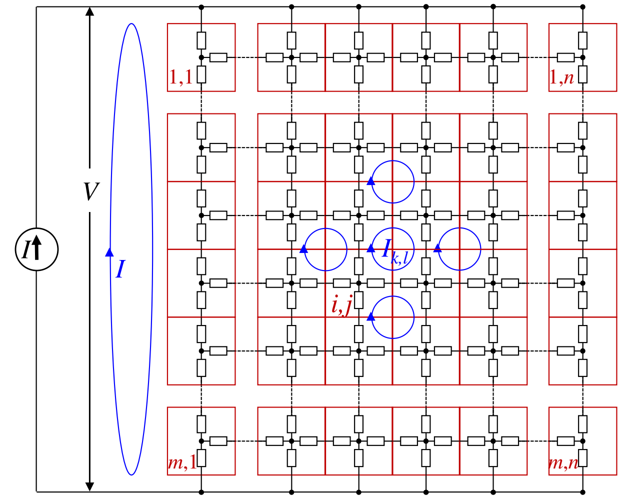


FIG. 8. The resistor network of $m \times n$ primitive cells used to approximate the resistance of the sample. Each primitive cell (red squares) contains one node and four resistors (except for the columns $j = 1$ and $j = n$, with only three resistors per primitive cell). A mesh current $I_{k,l}$ (blue) flows in each of the essential meshes of the resistor network. An additional mesh containing the current source is connected to the left-hand side of the resistor network.

can be written in matrix form as

$$\mathbf{W} \cdot \begin{pmatrix} I_{11} \\ \vdots \\ I_{1,n-1} \\ \vdots \\ I_{m+1,n-1} \\ I \end{pmatrix} = \begin{pmatrix} 0 \\ \vdots \\ 0 \\ \vdots \\ 0 \\ V \end{pmatrix}. \tag{B1}$$

The solution of this equation system returns, for a given bias current $I$, the voltage $V$ across the network and the mesh currents, from which the current through each of the four resistors in the primitive cell $i,j$ can be calculated according to

$$\begin{aligned} I_{i,j,1} &= I_{k,l} - I_{k,l-1}, \\ I_{i,j,2} &= I_{k+1,l} - I_{k,l}, \\ I_{i,j,3} &= I_{k+1,l} - I_{k+1,l-1}, \\ I_{i,j,4} &= I_{k+1,l-1} - I_{k,l-1}, \end{aligned} \tag{B2}$$

where, by convention, currents flowing in the positive $x$ and $y$ directions have positive sign. These describe the current flow between adjacent primitive cells and are defined on the boundary between them (cf. Fig. 9).

Although it is not properly defined, it is desirable to evaluate the current density at the nodes. This is calculated by interpolating the current densities at the boundaries of the primitive cell, which delivers the current densities $J^x_{i,j}$

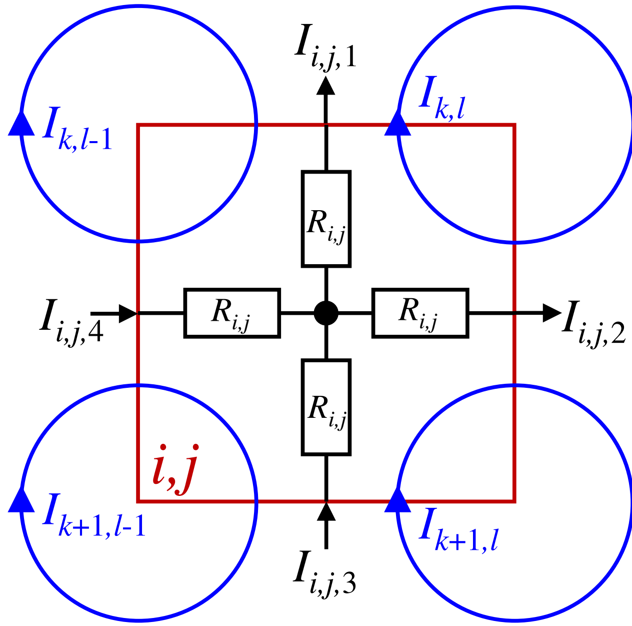


FIG. 9. On the definition of the currents $I_{i,j,1}$ to $I_{i,j,4}$ flowing through the resistors in the primitive cell $i,j$, which are calculated from the adjacent mesh currents.

in the $x$ direction and $J^{y}_{i,j}$ in the $y$ direction, as well as the magnitude of the current density $J^{\text{norm}}_{i,j}$:

$$J^{x}_{i,j} = \frac{I_{i,j,2} + I_{i,j,4}}{2\,\Delta y\, d_f},$$
$$J^{y}_{i,j} = \frac{I_{i,j,1} + I_{i,j,3}}{2\,\Delta x\, d_f},$$
$$J^{\text{norm}}_{i,j} = \sqrt{\left(J^{x}_{i,j}\right)^2 + \left(J^{y}_{i,j}\right)^2}, \tag{B3}$$

with the film thickness $d_f$. Note that these quantities approach the correct value only for $\Delta x$, $\Delta y \to 0$ and might deviate from the correct solution for finite dimensions of the primitive cell. Therefore, they are only used for displaying the results and not as input for further calculations. The power density $p_{i,j}$ generated through Joule heating in the primitive cell of volume $V_{i,j}$ is a quantity that is used for modeling the thermal characteristics of the sample and is given by

$$p_{i,j} = \frac{P_{i,j}}{V_{i,j}} = \frac{R_{ij}}{\Delta x\ \Delta y\ d_f}\left(I^2_{i,j,1} + I^2_{i,j,2} + I^2_{i,j,3} + I^2_{i,j,4}\right). \tag{B4}$$

For the reasons mentioned above, the currents through the boundaries are used to calculate the power dissipated in the resistors within the primitive cell.

### 2. Definition of temperature-dependent resistivity

To approximate the temperature dependence of the resistivity of the $V_2O_3$ film, the following assumptions are made. (i) The resistivity $\rho_{\text{met}}$ in the metallic phase is constant with respect to temperature and lateral position. (ii) The resistivity $\rho_{\text{ins}}$ deep in the insulating phase (at temperatures far below the MIT-IMT temperatures) is homogeneous and has the same temperature dependence as the globally measured $R(T)$. (iii) For cool-down of the sample, the increase in resistivity from $\rho_{\text{met}}$ to $\rho_{\text{ins}}$ in the transition region is described by a function $f\ (T_{\text{MIT}}(x,y) - T)$ that increases from 0 above the MIT temperature $T_{\text{MIT}}$ to 1 at low temperatures. Accordingly, the local resistivity for cool-down of the sample is described by the function

$$\rho_{\text{MIT}}(x,y,T) = \rho_{\text{ins}}(T)\ f\ [T_{\text{MIT}}(x,y) - T] + \rho_{\text{met}}. \tag{B5}$$

(iv) Similarly, for warm-up of the sample, the decrease in resistivity in the transition region is described by the same function $f\ [T_{\text{IMT}}(x,y) - T]$, which now has the difference between the IMT temperature $T_{\text{IMT}}$ and the temperature as argument:

$$\rho_{\text{IMT}}(x,y,T) = \rho_{\text{ins}}(T)\ f\ [T_{\text{IMT}}(x,y) - T] + \rho_{\text{met}}. \tag{B6}$$

Since the transition temperatures vary spatially, this leads to an inhomogeneous distribution of the resistivity in the transition region, while the resistivity is homogeneous outside the transition region. Note that the transition temperatures $T_{\text{MIT}}(x,y)$ and $T_{\text{IMT}}(x,y)$ that are used here to define the temperature dependence of the resistivity are determined experimentally (cf. Fig. 2), which should allow for a good representation of the spatial dependence of the resistivity.

The resistivity in the metallic phase is derived from experimental data as $\rho_{\text{met}} = 4.618 \times 10^{-6}$ Ωm. The resistivity at low temperatures is obtained by fitting the measured $R(T)$ curve in the temperature range from 80 K to 130 K with the function

$$\rho_{\text{ins}}(T) = ae^{bT} + ce^{dT}, \tag{B7}$$

where $a = 4.66 \times 10^{8}$ Ωm, $b = -0.1926$/K, $c = 3.19 \times 10^{5}$ Ωm, and $d = -0.09849$ /K. The function $f$ that describes the transition between the metallic and insulating phases is obtained by running the mesh-current analysis with the matrix $R_{i,j}(T)$ as input for temperatures throughout the transition region and adjusting $f$ until the measured resistance is reproduced. The resulting temperature-dependent resistivity is shown in Fig. 10.

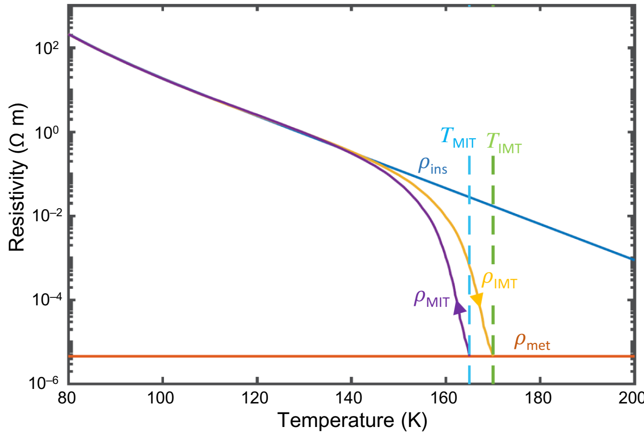


FIG. 10. The modeling of the temperature dependence of the $V_2O_3$ resistivity. For the cooling branch, $\rho_{MIT}$ increases from $\rho_{met}$ to $\rho_{ins}$ for $T < T_{MIT}$ (blue dashed line). In the heating branch $\rho_{IMT}$ decreases to $\rho_{met}$ for $T$ approaching $T_{IMT}$ (green dashed line).

### 3. Finite-difference approximation to heat equation

Heat transfer in solids is described by the parabolic partial differential equation, known as the heat equation:

$$\rho\, c_P \frac{\partial T}{\partial t} - \nabla\,(k \nabla T) = \dot{q}_V, \tag{B8}$$

where $\rho$ is the density, $c_P$ is the heat capacity at constant pressure, $k$ is the thermal conductivity, and $\dot{q}_V$ is the volumetric heat source. In two dimensions and for a film thickness $d_f$, this can be written as

$$\rho\, c_P \frac{\partial T}{\partial t} - \frac{\partial}{\partial x}\left(k_x \frac{\partial T}{\partial x}\right) - \frac{\partial}{\partial y}\left(k_y \frac{\partial T}{\partial y}\right) = \dot{q}_V, \tag{B9}$$

or, if the thermal conductivity $k = k_x = k_y$ is isotropic, as

$$\frac{\partial T}{\partial t} - \kappa\left(\frac{\partial^2 T}{\partial x^2} + \frac{\partial^2 T}{\partial y^2}\right) = \frac{\dot{q}_V}{\rho c_P}, \tag{B10}$$

where the thermal diffusivity $\kappa = k/(\rho c_P)$. The partial derivatives in the heat equation can be approximated by finite differences. The same discretization in space as for the mesh-current analysis is used and the variables are evaluated on the central node of the primitive cell with index $i, j$. The time is discretized into time steps $\Delta t$ and an index $\tau$ is introduced describing the point in time. The heat equation can be approximated in space and time using a number of finite-difference methods. Here, the backward Euler method is used which, in contrast to the forward Euler or Crank-Nicolson method, is unconditionally stable and immune to oscillations. For a node spacing of $\Delta x$ and $\Delta y$ and a time step $\Delta t$, the implicit discrete form of Eq. (B10) is given by

$$\frac{T_{i,j}^{\tau+1} - T_{i,j}^{\tau}}{\Delta t} - \kappa\left[\frac{T_{i,j+1}^{\tau+1} - 2T_{i,j}^{\tau+1} + T_{i,j-1}^{\tau+1}}{(\Delta x)^2} + \frac{T_{i+1,j}^{\tau+1} - 2T_{i,j}^{\tau+1} + T_{i-1,j}^{\tau+1}}{(\Delta y)^2}\right] = \frac{\dot{q}_{i,j}^{\tau}}{\rho\, c_P}. \tag{B11}$$

At this point, an additional thermal coupling to the bath with temperature $T_b$ is introduced, which is a consequence of the heat flow to the cold finger through the substrate of thickness $d_s$ and an effective thermal conductivity $k_s$. This can be modeled as a heat source $\dot{Q}_b = k_s\left(T_b - T_{i,j}^{\tau+1}\right)\, \Delta x \Delta y / d_s$ that is given by the power that is transferred to the bath through a cuboid with cross section $\Delta x\ \Delta y$ and length $d_s$. Accordingly, the volumetric heat source in Eq. (B11) is represented by the sum of Joule heating $p_{i,j}$ and a contribution of $\dot{Q}_b$ lumped to the volume $V_{i,j}$:

$$\dot{q}_{i,j}^{\tau} = p_{i,j}^{\tau} + \frac{\dot{Q}_b}{V_{i,j}} = p_{i,j}^{\tau} + \frac{k_s}{d_f\, d_s}\left(T_b - T_{i,j}^{\tau+1}\right). \tag{B12}$$

It is further assumed that the node spacing in the $x$ and $y$ directions is equal ($\Delta x = \Delta y$). With the thermal diffusivity to the bath $\kappa_s = k_s/\left(\rho_s\, c_{P,s}\right)$, Eq. (B11) becomes

$$T_{i,j}^{\tau+1} - T_{i,j}^{\tau} - \frac{\kappa\ \Delta t}{(\Delta x)^2} \times \left(T_{i-1,j}^{\tau+1} + T_{i,j-1}^{\tau+1} - 4T_{i,j}^{\tau+1} + T_{i,j+1}^{\tau+1} + T_{i+1,j}^{\tau+1}\right) = \frac{p_{i,j}^{\tau}\ \Delta t}{\rho\ c_P} + \frac{\kappa_s\ \Delta t}{d_f\ d_s}\left(T_b - T_{i,j}^{\tau+1}\right). \tag{B13}$$

Rearranging this equation so that terms at time $\tau + 1$ are on the left-hand side and terms at time $\tau$ are on the right-hand side, and introducing the coefficients $A_f = \kappa\ \Delta t/(\Delta x)^2$, $A_b = \kappa_s\ \Delta t/\left(d_f\ d_s\right)$, and $A_q = \Delta t/(\rho\ c_P)$, results in

$$-A_f\ T_{i-1,j}^{\tau+1} - A_f\ T_{i,j-1}^{\tau+1} + \left(1 + 4A_f + A_b\right) T_{i,j}^{\tau+1} - A_f\ T_{i,j+1}^{\tau+1} - A_f\ T_{i+1,j}^{\tau+1} - A_b T_b = T_{i,j}^{\tau} + A_q p_{i,j}^{\tau}. \tag{B14}$$

These equations are assembled into a $(m \cdot n + 1) \times (m \cdot n + 1)$ heat transfer matrix $\mathbf{H}$ so that the equation system is given by

$$\mathbf{H} \cdot \begin{pmatrix} T_{11}^{\tau+1} \\ \vdots \\ T_{1n}^{\tau+1} \\ \vdots \\ T_{mn}^{\tau+1} \\ T_b \end{pmatrix} = \begin{pmatrix} T_{11}^{\tau} + A_q p_{1,1}^{\tau} \\ \vdots \\ T_{1n}^{\tau} + A_q p_{1,n}^{\tau} \\ \vdots \\ T_{mn}^{\tau} + A_q p_{m,n}^{\tau} \\ T_{\text{bath}} \end{pmatrix}, \tag{B15}$$

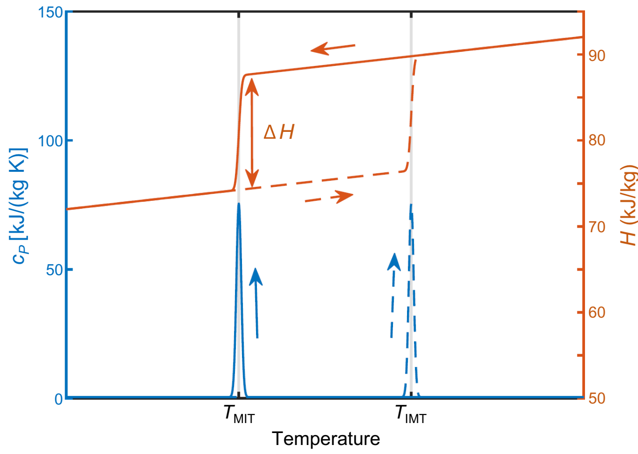


FIG. 11. The temperature-dependent heat capacity $c_P$ (blue curve) and enthalpy $H$ (red curve). The latent heat $\Delta H$ at the phase transition leads to a jump in enthalpy and a peak in heat capacity. The broken lines show the IMT at $T_{\mathrm{IMT}}$ and the solid lines the MIT at $T_{\mathrm{MIT}}$.

where the last row contains the equation $T_b = T_{\mathrm{bath}}$, which is used to set the bath temperature as a boundary condition.

The metal-insulator phase transition in $V_2O_3$ is connected to the occurrence of a latent heat of approximately $\Delta H = 2$ kJ/mol $\approx 13.3$ kJ/kg that has to be supplied to the system to change from one phase to the other [62]. The latent heat, which is represented by a jump in enthalpy $H$, leads to a diverging heat capacity $c_P = dH/dT$ at the phase transition [63]. The latent heat is represented in the numerical model by introducing a temperature-dependent heat capacity

$$c_P(T) = c_{P0} + \frac{\Delta H}{\sqrt{\pi}\,\Delta T} e^{\frac{(T-T_c)^2}{\Delta T^2}}, \tag{B16}$$

where a constant heat capacity $c_{P0} = 0.45$ kJ/ (kg K) and a finite width $\Delta T = 0.1$ K of the phase transition around the transition temperature $T_c$ is assumed. The heat capacity according to Eq. (B16) is shown in Fig. 11.

#### 4. Simulation of electrical breakdown in $V_2O_3$

To simulate the electrical breakdown in $V_2O_3$, the equations for the current distribution and heat transfer [Eqs. (B1) and (B15), respectively] are implemented and solved in MATLAB. This is done by initializing the system at zero bias current ($I_{\mathrm{bias}} = 0$) and at the bath temperature ($T_{i,j} = T_{\mathrm{bath}}$) for $t = 0$ and slowly ramping the current to $I_{\mathrm{bias}}^{\mathrm{max}} = 20$ mA and back to $I_{\mathrm{bias}}^{\mathrm{end}} = 0$ mA over time, with a rate that is much slower than the thermal dynamics of the sample, so that the system is modeled in quasistatic approximation.

Figure 12 shows the program flow chart. First, the system is initialized at the bath temperature, zero bias current, and completely in the insulating phase. Then, the $R_{i,j}$ for

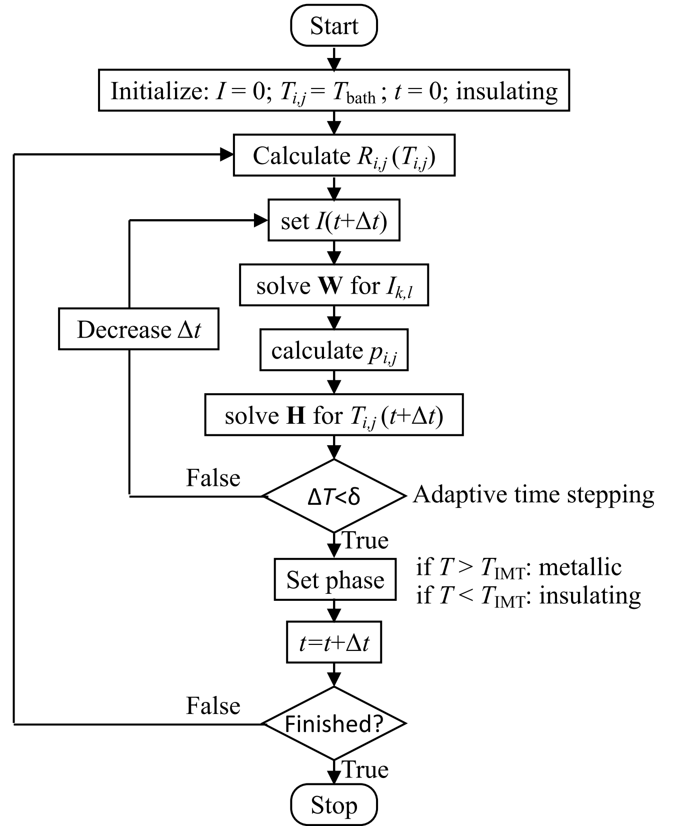


FIG. 12. The flow chart for the simulation.

the initial temperature and phase are calculated. The bias current is increased to the value at the next time step, $t + \Delta t$. The mesh-current analysis is solved and the current distribution is calculated. The Joule heating is calculated from $R_{i,j}$ and the current distribution and input into the heat equation, which is solved for the temperatures $T_{i,j}\,(t + \Delta t)$. Note that due to the strong temperature dependence of resistivity and heat capacity, the system is highly nonlinear as it approaches the MIT or IMT. To accurately capture the nonlinearities, a sufficiently small time step $\Delta t$ needs to be used. This is accomplished by using an adaptive time step. If the maximum change in temperature,

$$\Delta T = \max_{\forall i,j}\left[\left|T_{i,j}\,(t+\Delta t) - T_{i,j}\,(t)\right|\right], \tag{B17}$$

is larger than the convergence criterion $\delta$, the time step is reduced and the temperature distribution is recalculated using the smaller time step. If $\Delta T$ is far below the convergence criterion, the time step is increased. When the convergence criterion is satisfied, the phase transition is evaluated: the material is set to the metallic phase, where $T_{\mathrm{IMT}}$ is exceeded and to the insulating phase, where the temperature has fallen below $T_{\mathrm{MIT}}$. Subsequently, the time is incremented and the calculated temperature and phase

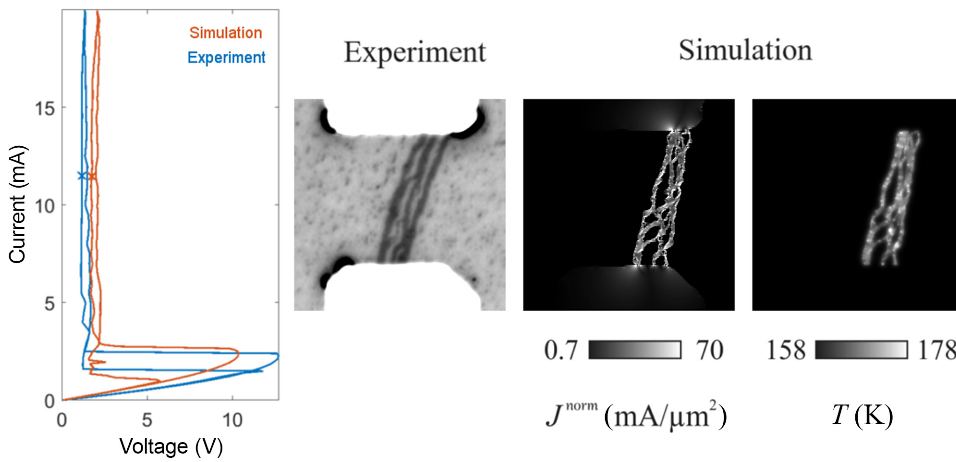


VIDEO 1. An animation of the electrical breakdown in a planar thin-film device at the onset of the IMT. The left-hand graph shows the current-voltage relation of the experiment and the simulation. The two small crosses ("×") mark the bias points. The panel in the center shows the corresponding photomicrographs of the device under investigation. The two panels on the right-hand side show the simulated current density and temperature.

distribution are used as inputs to calculate the new $R_{i,j}$ values. The program runs in a loop, progressing through time, until the bias current has reached its final value.

## APPENDIX C: CURRENT-VOLTAGE RELATION, PHOTOMICROGRAPHS, AND COMPUTER-SIMULATION DATA COMBINED IN ONE ANIMATION

To summarize the main results on resistive switching due to electrothermal filament formation, we combine the electrical transport measurement data, the photomicrographs, and the computer-simulation data in one animation (see Video 1).


[1] P. Limelette, A. Georges, D. Jérome, P. Wzietek, P. Metcalf, and J. M. Honig, Universality and critical behavior at the Mott transition, Science **302**, 89 (2003).

[2] D. B. McWhan and J. P. Remeika, Metal-insulator transition in $(V_{1-x}Cr_x)_2O_3$, Phys. Rev. B **2**, 3734 (1970).

[3] M. Imada, A. Fujimori, and Y. Tokura, Metal-insulator transitions, Rev. Mod. Phys. **70**, 1039 (1998).

[4] A. Singer, J. G. Ramirez, I. Valmianski, D. Cela, N. Hua, R. Kukreja, J. Wingert, O. Kovalchuk, J. M. Glownia, M. Sikorski, M. Chollet, M. Holt, I. K. Schuller, and O. G. Shpyrko, Nonequilibrium Phase Precursors during a Photoexcited Insulator-to-Metal Transition in $V_2O_3$, Phys. Rev. Lett. **120**, 207601 (2018).

[5] Z. Yang, C. Ko, and S. Ramanathan, Oxide electronics utilizing ultrafast metal-insulator transitions, Annu. Rev. Mater. Res. **41**, 337 (2011).

[6] P. Markov, R. E. Marvel, H. J. Conley, K. J. Miller, R. F. Haglund Jr., and S. M. Weiss, Optically monitored electrical switching in $VO_2$, ACS Photonics **2**, 1175 (2015).

[7] N. A. Butakov, I. Valmianski, T. Lewi, C. Urban, Z. Ren, A. A. Mikhailovsky, S. D. Wilson, I. K. Schuller, and J. A. Schuller, Switchable plasmonic-dielectric resonators with metal-insulator transitions, ACS Photonics **5**, 371 (2018).

[8] J. del Valle, Y. Kalcheim, J. Trastoy, A. Charnukha, D. N. Basov, and I. K. Schuller, Electrically Induced Multiple Metal-Insulator Transitions in Oxide Nanodevices, Phys. Rev. Appl. **8**, 054041 (2017).

[9] E. Janod, J. Tranchant, B. Corraze, M. Querré, P. Stoliar, M. Rozenberg, T. Cren, D. Roditchev, V. T. Phuoc, M. Besland, and L. Cario, Resistive switching in Mott insulators and correlated systems, Adv. Funct. Mater. **25**, 6287 (2015).

[10] C.-Y. Lin, P.-H. Chen, T.-C. Chang, K.-C. Chang, S.-D. Zhang, T.-M. Tsai, C.-H. Pan, M.-C. Chen, Y.-T. Su, Y.-T. Tseng, Y.-F. Chang, Y.-C. Chen, H.-C. Huang, and S. M. Sze, Attaining resistive switching characteristics and selector properties by varying forming polarities in a single $HfO_2$-based RRAM device with a vanadium electrode, Nanoscale **9**, 8586 (2017).

[11] A. Sawa, Resistive switching in transition metal oxides, Mater. Today **11**, 28 (2008).

[12] H. S. P. Wong, H.-Y. Lee, S. Yu, Y.-S. Chen, Y. Wu, P.-S. Chen, B. Lee, F. T. Chen, and M.-J. Tsai, Metal-oxide RRAM, Proc. IEEE **100**, 1951 (2012).

[13] M. A. Zidan, J. P. Strachan, and W. D. Lu, The future of electronics based on memristive systems, Nat. Electron. **1**, 22 (2018).

[14] D. Ielmini and H. S. P. Wong, In-memory computing with resistive switching devices, Nat. Electron. **1**, 333 (2018).

[15] Z. Wang, H. Wu, G. W. Burr, C. S. Hwang, K. L. Wang, Q. Xia, and J. J. Yang, Resistive switching materials for information processing, Nat. Rev. Mater. **5**, 173 (2020).

[16] M. D. Pickett, G. Medeiros-Ribeiro, and R. S. Williams, A scalable neuristor built with Mott memristors, Nat. Mater. **12**, 114 (2013).

[17] I. K. Schuller, R. Stevens, R. Pino, and M. Pechan, Neuromorphic computing—from materials research to systems architecture roundtable, DOI:10.2172/1283147 (2015).

[18] P. Stoliar, J. Tranchant, B. Corraze, E. Janod, M. Besland, F. Tesler, M. Rozenberg, and L. Cario, A leaky-integrate-and-fire neuron analog realized with a Mott insulator, Adv. Funct. Mater. **27**, 1604740 (2017).

[19] W. Yi, K. Tsang, S. Lam, X. Bai, J. Crowell, and E. Flores, Biological plausibility and stochasticity in scalable $VO_2$ active memristor neurons, Nat. Commun. **9**, 4661 (2018).

[20] J. del Valle, P. Salev, F. Tesler, N. M. Vargas, Y. Kalcheim, P. Wang, J. Trastoy, M.-H. Lee, G. Kassabian, J. G. Ramírez, M. J. Rozenberg, and I. K. Schuller, Subthreshold firing in Mott nanodevices, Nature **569**, 388 (2019).

[21] Hai-Tian Zhang, Priyadarshini Panda, Jerome Lin, Yoav Kalcheim, Kai Wang, John Freeland, Dillon Fong, Shashank Priya, Ivan Schuller, Subramanian Sankaranarayanan, Kaushik Roy, and Shriram Ramanathan, Organismic materials for beyond von Neumann machines, Appl. Phys. Rev. **7**, 011309 (2020).

[22] Sangheon Oh, Yuhan Shi, Javier del Valle, Pavel Salev, Yichen Lu, Zhisheng Huang, Yoav Kalcheim, Ivan K. Schuller, and Duygu Kuzum, Energy-efficient Mott activation neuron for full-hardware implementation of neural networks, Nat. Nanotechnol. **16**, 680 (2021).

[23] T. Oka, R. Arita, and H. Aoki, Breakdown of a Mott Insulator: A Nonadiabatic Tunneling Mechanism, Phys. Rev. Lett. **91**, 066406 (2003).

[24] H. Yamakawa, T. Miyamoto, T. Morimoto, T. Terashige, H. Yada, N. Kida, M. Suda, H. M. Yamamoto, R. Kato, K. Miyagawa, K. Kanoda, and H. Okamoto, Mott transition by an impulsive dielectric breakdown, Nat. Mater. **16**, 1100 (2017).

[25] T. Oka and H. Aoki, Ground-State Decay Rate for the Zener Breakdown in Band and Mott Insulators, Phys. Rev. Lett. **95**, 137601 (2005).

[26] M. Eckstein, T. Oka, and P. Werner, Dielectric Breakdown of Mott Insulators in Dynamical Mean-Field Theory, Phys. Rev. Lett. **105**, 146404 (2010).

[27] F. Heidrich-Meisner, I. González, K. A. Al-Hassanieh, A. E. Feiguin, M. J. Rozenberg, and E. Dagotto, Nonequilibrium electronic transport in a one-dimensional Mott insulator, Phys. Rev. B **82**, 205110 (2010).

[28] R. Kumai, Y. Okimoto, and Y. Tokura, Current-induced insulator-metal transition and pattern formation in an organic charge-transfer complex, Science **284**, 1645 (1999).

[29] S. Yamanouchi, Y. Taguchi, and Y. Tokura, Dielectric Breakdown of the Insulating Charge-Ordered State in $La_{2-x}Sr_xNiO_4$, Phys. Rev. Lett. **83**, 5555 (1999).

[30] I. Valmianski, P. Y. Wang, S. Wang, J. G. Ramírez, S. Guénon, and I. K. Schuller, Origin of the current-driven breakdown in vanadium oxides: Thermal versus electronic, Phys. Rev. B **98**, 195144 (2018).

[31] W.-R. Lee and K. Park, Dielectric breakdown via emergent nonequilibrium steady states of the electric-field-driven Mott insulator, Phys. Rev. B **89**, 205126 (2014).

[32] N. Sugimoto, S. Onoda, and N. Nagaosa, Field-induced metal-insulator transition and switching phenomenon in correlated insulators, Phys. Rev. B **78**, 155104 (2008).

[33] G. Mazza, A. Amaricci, M. Capone, and M. Fabrizio, Field-Driven Mott Gap Collapse and Resistive Switch in Correlated Insulators, Phys. Rev. Lett. **117**, 176401 (2016).

[34] J. Li, C. Aron, G. Kotliar, and J. E. Han, Electric-Field-Driven Resistive Switching in the Dissipative Hubbard Model, Phys. Rev. Lett. **114**, 226403 (2015).

[35] J. Duchene, M. Terraillon, P. Pailly, and G. Adam, Filamentary conduction in $VO_2$ coplanar thin-film devices, Appl. Phys. Lett. **19**, 115 (2003).

[36] S. Guénon, S. Scharinger, S. Wang, J. G. Ramírez, D. Koelle, R. Kleiner, and I. K. Schuller, Electrical breakdown in a $V_2O_3$ device at the insulator-to-metal transition, EPL **101**, 57003 (2013).

[37] J. S. Brockman, L. Gao, B. Hughes, C. T. Rettner, M. G. Samant, K. P. Roche, and S. S. P. Parkin, Subnanosecond incubation times for electric-field-induced metallization of a correlated electron oxide, Nat. Nanotechnol. **9**, 453 (2014).

[38] V. I. Polozov, S. S. Maklakov, A. L. Rakhmanov, S. A. Maklakov, and V. N. Kisel, Blow-up overheating instability in vanadium dioxide thin films, Phys. Rev. B **101**, 214310 (2020).

[39] Manca, *et al.*, Influence of thermal boundary conditions on the current-driven resistive transition in $VO_2$ microbridges, Appl. Phys. Lett. **107**, 143509 (2015).

[40] Javier Del Valle, Nicolas M. Vargas, Rodolfo Rrocco, Pavel Salevyoav Kalcheim, Pavel N. Lapa, Coline Adda, Min-Han Lee, Paul y. Wang, Lorenzo Fratino, Marcelo L. Rozenberg, and Ivan K. Schuller, Spatiotemporal characterization of the field-induced insulator-to-metal transition, Science **373**, 907 (2021).

[41] A. V. Gurevich and R. G. Mints, Self-heating in normal metals and superconductors, Rev. Mod. Phys. **59**, 941 (1987).

[42] F. Giorgianni, J. Sakai, and S. Lupi, Overcoming the thermal regime for the electric-field driven Mott transition in vanadium sesquioxide, Nat. Commun. **10**, 1159 (2019).

[43] Y. Kalcheim, A. Camjayi, J. del Valle, P. Salev, M. Rozenberg, and I. K. Schuller, Non-thermal resistive switching in Mott insulator nanowires, Nat. Commun. **11**, 2985 (2020).

[44] H. Schuler, S. Klimm, G. Weissmann, C. Renner, and S. Horn, Influence of strain on the electronic properties of epitaxial $V_2O_3$ thin films, Thin Solid Films **299**, 119 (1997).

[45] N. Alyabyeva, J. Sakai, M. Bavencoffe, J. Wolfman, P. Limelette, H. Funakubo, and A. Ruyter, Metal-insulator transition in $V_2O_3$ thin film caused by tip-induced strain, Appl. Phys. Lett. **113**, 241603 (2018).

[46] A. Ronchi, P. Homm, M. Menghini, P. Franceschini, F. Maccherozzi, F. Banfi, G. Ferrini, F. Cilento, F. Parmigiani, S. S. Dhesi, M. Fabrizio, J.-P. Locquet, and C. Giannetti, Early-stage dynamics of metallic droplets embedded in the nanotextured Mott insulating phase of $V_2O_3$, Phys. Rev. B **100**, 075111 (2019).

[47] Yoav Kalcheim, Nikita Butakov, Nicolas M. Vargas, Min-Han Lee, Javier del Valle, Juan Trastoy, Pavel Salev, Jon Schuller, and Ivan K. Schuller, Robust Coupling between Structural and Electronic Transitions in a Mott Material, Phys. Rev. Lett. **122**, 057601 (2019).

[48] Yoav Kalcheim, Coline Adda, Pavel Salev, Min-Han Lee, Nareg Ghazikhanian, Nicolás M. Vargas, Javier del Valle, and Ivan K. Schuller, Structural Manipulation of Phase Transitions by Self-Induced Strain in Geometrically Confined Thin Films, Adv. Funct. Mater. **30**, 2005939 (2020).

[49] Pavel Salev, Javier del Valle, Yoav Kalcheim, and Ivan K. Schuller,Giant nonvolatile resistive switching in a Mott oxide and ferroelectric hybrid, PNAS **116**, 8798 (2019).

[50] A. S. McLeod, E. van Heumen, J. G. Ramírez, S. Wang, T. Saerbeck, S. Guénon, M. Goldflam, L. Anderegg, P. Kelly, A. Mueller, M. K. Liu, I. K. Schuller, and D. N. Basov, Nanotextured phase coexistence in the correlated insulator $V_2O_3$, Nat. Phys. **13**, 80 (2017).

[51] P. Stoliar, L. Cario, E. Janod, B. Corraze, C. Guillot-Deudon, S. Salmon-Bourmand, V. Guiot, J. Tranchant, and M. Rozenberg, Universal electric-field-driven resistive transition in narrow-gap Mott insulators, Adv. Mater. **25**, 3222 (2013).

[52] P. Diener, E. Janod, B. Corraze, M. Querré, C. Adda, M. Guilloux-Viry, S. Cordier, A. Camjayi, M. Rozenberg, M. P. Besland, and L. Cario, How a dc Electric Field Drives Mott Insulators out of Equilibrium, Phys. Rev. Lett. **121**, 016601 (2018).

[53] G. Gopalakrishnan, D. Ruzmetov, and S. Ramanathan, On the triggering mechanism for the metal-insulator transition in thin film $VO_2$ devices: Electric field versus thermal effects, J. Mater. Sci. **44**, 5345 (2009).

[54] A. Ronchi, P. Franceschini, P. Homm, M. Gandolfi, G. Ferrini, S. Pagliara, F. Banfi, M. Menghini, J.-P. Locquet, and C. Giannetti, Light-Assisted Resistance Collapse in a $V_2O_3$-Based Mott-Insulator Device, Phys. Rev. Appl. **15**, 044023 (2021).

[55] M. K. Stewart, D. Brownstead, S. Wang, K. G. West, J. G. Ramirez, M. M. Qazilbash, N. B. Perkins, I. K. Schuller, and D. N. Basov, Insulator-to-metal transition and correlated metallic state of $V_2O_3$ investigated by optical spectroscopy, Phys. Rev. B **85**, 205113 (2012).

[56] J. Trastoy, Y. Kalcheim, J. del Valle, I. Valmianski, and Ivan K. Schuller, Enhanced metal-insulator transition in $V_2O_3$ by thermal quenching after growth, J. Mater. Sci. **53**, 9131 (2018).

[57] M. Lange, S. Guénon, F. Lever, R. Kleiner, and D. Koelle, A high-resolution combined scanning laser- and widefield polarizing microscope for imaging at temperatures from 4 K to 300 K, Rev. Sci. Instr. **88**, 123705 (2017).

[58] A. I. Poteryaev, J. M. Tomczak, S. Biermann, A. Georges, A. I. Lichtenstein, A. N. Rubtsov, T. Saha-Dasgupta, and O. K. Andersen, Enhanced crystal-field splitting and orbital-selective coherence induced by strong correlations in $V_2O_3$, Phys. Rev. B **76**, 085127 (2007).

[59] S.-K. Mo, J. D. Denlinger, H.-D. Kim, J.-H. Park, J. W. Allen, A. Sekiyama, A. Yamasaki, K. Kadono, S. Suga, Y. Saitoh, T. Muro, P. Metcalf, G. Keller, K. Held, V. Eyert, V. I. Anisimov, and D. Vollhardt, Prominent Quasiparticle Peak in the Photoemission Spectrum of the Metallic Phase of $V_2O_3$, Phys. Rev. Lett. **90**, 186403 (2003).

[60] H. Garcke and U. Weikard, Numerical approximation of the Cahn-Larché equation, Numer. Math. **100**, 639 (2005).

[61] M. Lange, Ph.D. thesis, Eberhard Karls Universität Tübingen, 2018.

[62] H. V. Keer, D. L. Dickerson, H. Kuwamoto, H. L. C. Barros, and J. M. Honig, Heat capacity of pure and doped $V_2O_3$ single crystals, J. Solid State Chem. **19**, 95 (1976).

[63] O. V. Lyakh, V. I. Surikov, V. I. Surikov, and N. A. Prokudina, Magnetic susceptibility and heat capacity of $V_2O_3$ and $V_{1.973}Me_{0.020}O_3$ (Me = Fe, Cr and Al), Russ. Phys. J **55**, 116 (2012).